Optical Materials: X 20 (2023) 100273

Contents lists available at ScienceDirect

Optical Materials: X

journal homepage: www.elsevier.com/locate/omx

Understanding the coupling between MIM cavities due to single and double Tamm plasmon polaritons

Leandro Luis Missoni [a,b], Guillermo Pablo Ortiz [c], María Luz Martínez Ricci [a,*]

[a] Instituto de Química Física de los Materiales, Medio Ambiente y Energía (INQUIMAE), CONICET, Universidad de Buenos Aires, Ciudad Universitaria, Pab. II, Ciudad Autónoma de Buenos Aires, Argentina

[b] Departamento de Química Inorgánica, Analítica y Química Física, Facultad de Ciencias Exactas y Naturales, Universidad de Buenos Aires, Ciudad Universitaria, Pab. II, Ciudad Autónoma de Buenos Aires, Argentina

[c] Departamento de Física, Facultad de Ciencias Exactas, Naturales y Agrimensura, Universidad Nacional del Nordeste, Corrientes, Argentina

ARTICLE INFO

Keywords:
TAMM plasmon polaritons
Strong-coupling
Photonic crystals
MIM structures

ABSTRACT

The interplay between light and matter plays a crucial role in various applications, ranging from sensor technologies to integrated optoelectronic architectures. In this contribution, a systematic numerical study is made over the symmetry role of the 1D photonic structures (PhSs) containing a low number of slabs embedded in thin metal layers, in order to find the adequate conditions to enhance the quality factor of resonances and energy confinement in the subwavelength scale. We show the existence of single and double Tamm plasmon polaritons (TPPs) states according to the symmetry of the PhS, which allow to tune weak and strong coupling regimes with Metal–Insulator–Metal (MIM) platforms combined in a unique MIM-PhS-MIM structure. We found that while weak coupling is observable between MIM and PhS states at the PhS cavity mode wavelengths, strong coupling among the 2 MIMs and the PhS is obtained only at the TPP resonance wavelengths, exhibited by anti-crossing splittings at adequate insulator thicknesses. We found that for the double Tamm plasmon polaritons, the energy splitting can reach up to 134 meV, unlike the single TPPs where the maximum energy splitting is on the order of 50 meV. The degree of coupling was explained by the implementation of a variational method that exploits the analogy the optical superlattice herein proposed and an analogous superlattice quantum well. This article shows that TPP resonances are responsible for the coherent coupling between the two MIMs placed at a long distance given by the PhSs. Thus, these platforms provide an interesting and experimentally accessible route for the coupling of emitters in optoelectronic devices.

1. Introduction

The possibility to concentrate light in confined photonic structures leading to sub-wavelength localization of optical energy is a high-interest research topic due from both a fundamental point of view [1–3] and also for potential applications which include lasing [4], SERS detection [5], photocatalysis [6], solar energy harvesting [7] or light-driven therapies [8]. The basis of these light concentrators is the design of resonant nanostructures which may include nanocavities as Fabry–Pérot (FP) ethalons [9,10], Photonic Crystals (PhCs) [11,12], Whispering Gallery Modes (WGMs) [13] or plasmon resonances as Surface Plasmon Polaritons (SPPs) [14]. The design and synthesis of these resonant and tunable nanostructures and their integration into other structures might not be easy to achieve requiring sophisticated equipment [15]. In this sense, the use of 1D stacked structures has the advantage of reaching to interesting hybrid nanostructures with easier synthesis procedures as classical sol–gel derived oxides [11,16,17], nanoparticles [18], or self-assembled polymers [19].

Metal–Insulator–Metal (MIM) 1D cavities have demonstrated to be excellent candidates for EM field confinement and enhancement since they present strong, sharp, and tunable cavity resonances which have been applied to diverse optical platforms, including electrically modulated color filters [20], non-linear optics [21] and applied into composed nanostructures creating hybrid systems. Caligiuri et al. [22] have studied the resonant modes of MIM cavities showing an epsilon-near-zero (ENZ) metamaterials behavior. Also they have shown the coupling between stacked MIM [23] structures forming MIMIM multicavities which present either weak and strong coupling hybridization modes which can lead to optical tunneling effects. Strong coupling has been deeply studied in quantum systems and arise from the strong interaction between two quantum states, it is observed whenever the coupling strength exceeds the dissipation rates of the systems, leading

* Corresponding author.
E-mail address: mricci@qi.fcen.uba.ar (M.L. Martínez Ricci).

https://doi.org/10.1016/j.omx.2023.100273
Received 18 August 2023; Received in revised form 25 September 2023; Accepted 27 September 2023
Available online 30 September 2023

to coherent phenomena. In the last years, strong coupling has also been observed in many photonic and plasmonic nanostructures generally involving nanocavities [24] leading a path towards light–matter interactions [25]. Zappone et al. [26] have shown experimentally weak coupling hybridization in a Surface Force Apparatus (SFA) and also proposed a semiclassical analysis of the splitting and coupling through the use of the Rayleigh–Ritz variational method typically employed to explain the hybridization in molecular quantum theory. The possibility to achieve and control the hybridization of states in particular in the strong coupling regime, also known as Rabi splitting, in plasmonics and photonics platforms is of interest due to the possibility of modifying the electromagnetic environment in the vicinity of an emitter [27]. SPPs, which are electromagnetic surface states at the interface between a metal and a dielectric, have been deeply studied and applied into many hybrid platforms because of their aforementioned ability to concentrate light at the dielectric with a characteristic exponential and rapid decay. The tuning of the SPP state is not trivial, requiring couplers as a prism or a diffraction grating for coupling the incident wave at a specific angle and polarization. However, many interesting strong coupling between SPPs and J-aggregates [28,29] or Quantum Dots [30] have been fulfilled.

More recently, another type of surface state with interesting and different characteristics is the Tamm Plasmon Polariton (TPP) which has been was firstly introduced by Kaliteevski et al. [31] in analogy to Tamm electron states [32]. TPPs appear at the interface of a metal thin slab with a 1D PhC, whenever the adequate impedance condition is fulfilled which restrings the appearance of TPP when the high refractive index material of the 1D PhC is next to the metal slab. Unlike SPP modes, TPP modes do not have specific requirements over angle of incidence, or polarization and fundamentally, do not need to be excited by using couplers. Due to the impedance conditions, the TPP resonance peak appears inside the band-gap of the PhC, and its sharpness is favored when high index of refraction contrast is available between the materials of the PhC slabs and also it increases with the number of unit cells of the PhC. These characteristics make TPP platforms promising for various optical applications as Tamm lasing [33], gas sensors [34,35] among others light–matter devices [36]. TPPs have also been applied to the design of hybrid platforms that exhibit strong coupling resonant modes interactions when it is combined with other cavities or defects included in the PhC [24,37]. It is important to denote that many of the designed platforms used to optimize the optical response or to obtain large Rabi splitting require a great number of layers or involve difficult deposition techniques.

Some experimental deposition techniques make it possible to synthesize in simple and fast synthesis procedures many useful devices, but typically do not allow the deposition of a high numberof slabs [11,35] what goes in detriment of the TPP sharpness. In this work, we numerically investigate how the symmetry order of the slabs that compose the photonic structure (PhS) improves the sharpness and the quality of the TPP resonance when the PhS has a low number of layers taking into consideration feasible experimental devices that could be fulfilled for example by Sol-Gel synthesis [34,35]. The TPP resonances when the PhS is embedded within 2 thin metal slabs, forming a PhS-FP cavity, are also detailed. In particular, we focus on two complementary aspects of TPP, one oriented to sensing applications, analyzing the sensibility and sharpness of the resonance for dense and porous structures and the other one, studying the localization and concentration of the electric field towards the use of these platforms as electromagnetic (EM) energy harvesters for photoactive nanoentities. In the second section of this manuscript, we take advantage of the symmetry analyzed and design hybrid MIM-PhS-MIM platforms to obtain a strong interplay between MIM states at the TPP resonant modes. We demonstrate that even with low number of layers, the symmetry of the PhS structure defines the characteristics of the Tamm resonant mode and regulates the Rabi splittings spectral responses. Finally, we propose an extension of the quantum analogy proposed by Zappone et al. to shade light on the phenomenology involved in the strong coupling regimes.

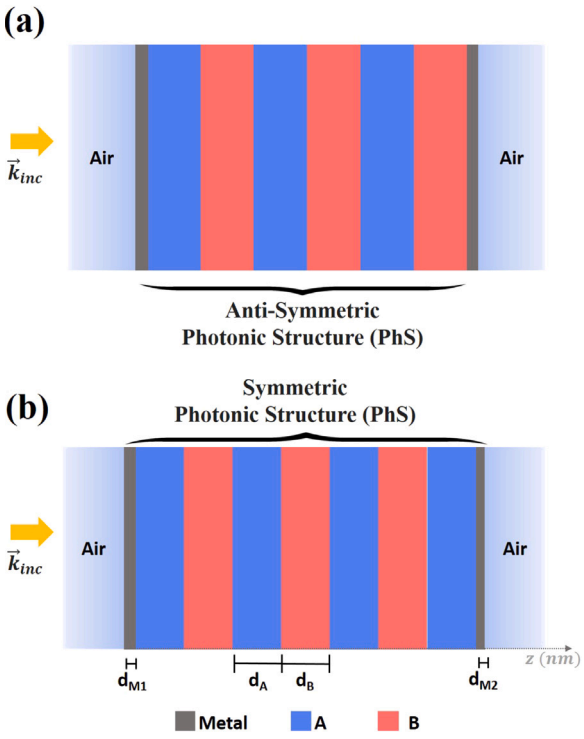

Fig. 1. Schemes of the 1D multilayer photonic structures M-PhC-M used in this work. The stack starts with a metal (Ag, gray) thin layer, which is followed by multilayer composed by two dielectrics with a low (blue) and high (red) refractive index, and finishes with another metal (Ag, gray) thin layer. (a) An anti-symmetric photonic structure, which contains an even number of layers and the first and last dielectric are not the same. (b) A symmetric photonic structure, which contains an odd number of layers and the first and last dielectric are the same. (For interpretation of the references to color in this figure legend, the reader is referred to the web version of this article.)

2. Structure design and simulation framework

A graphical illustration of the studied multilayered structure is depicted in Fig. 1. Multilayer composite is stacked in z-direction. It starts and finishes with a metal thin layer of variable thickness, namely d_{M_1} and d_{M_2} respectively. Within the metal layers, there is a PhS compose by alternating dielectrics, A and B slabs of thickness d_A and d_B. Fig. 1(a) shows an anti-symmetric structure while Fig. 1(b) adds an extra layer defining a symmetric photonic structure. For simulations, the two selected dielectrics have been SiO_2 and TiO_2 that have excellent optical response with no significant dissipation losses in the [400–2000] nm range with an adequate refractive index contrast between layer of the unit cell for a clear band-gap as already seen experimentally by the group using the sol–gel technique [11]. In all cases, SiO_2 corresponds to the low (L) refractive-index layer while TiO_2 is the high (H) refractive-index layer. Ag has been taken as metal thin layer at the beginning or end of the composed structure. Multilayers will be denoted as $(AB)_n$ for anti-symmetric structures of n bilayers while $(AB)_nA$ will refer to symmetric structures composed of n AB bilayers that finish with a final A layer. When the structure initiates or finishes with a metal thin layer a M will be added to the structure. For instance a M-$(AB)_3$-M will refer to a structure that initiates with a metal thin film, then follows with an anti-symmetric structure of 3 AB bilayers and finishes with another metal thin film. Refractive index data employed in this work correspond to the well-known reference of Johnson and Christy [38] for

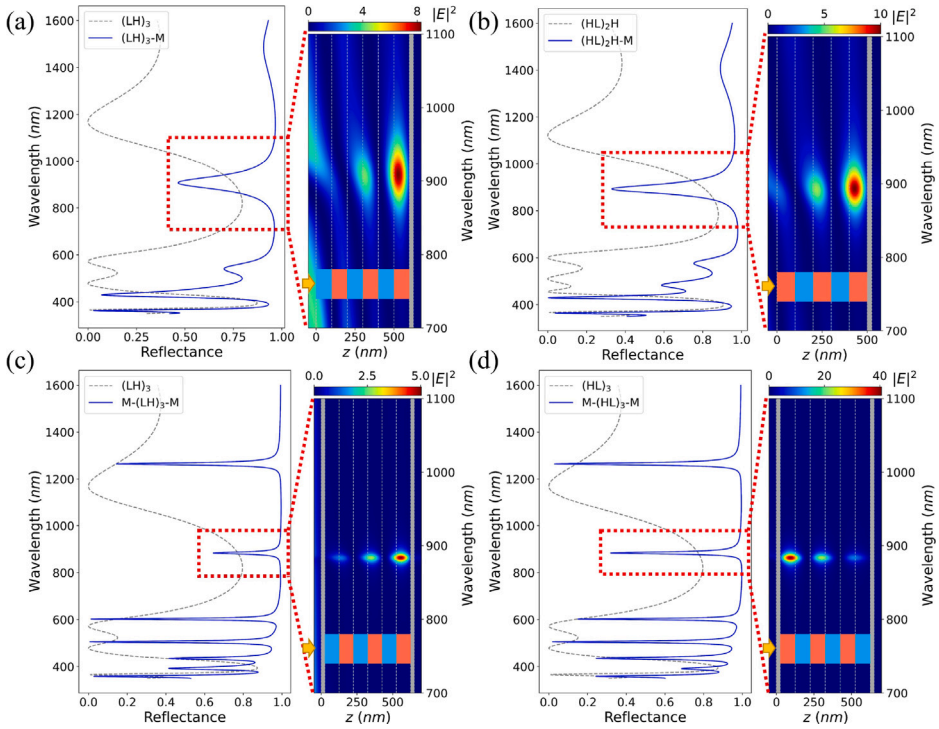

Fig. 2. Reflectance spectra simulated for several M-PhS-M structures (blue line) and $|\mathbb{E}|^2$ distribution at some resonances. In dashed gray line, the reflectance spectra of isolated photonic structure, without metal layers, is plotted. (a) $(LH)_3$-M structure. (b) $(HL)_2$H-M structure. (c) M-$(LH)_3$-M structure. (d) M-$(HL)_3$-M structure. (For interpretation of the references to color in this figure legend, the reader is referred to the web version of this article.)

the Ag film while SiO_2 and TiO_2 refractive indexes have been nominally taken from [39,40] respectively considering in all three materials their dispersive character. In all studied cases, dielectric thicknesses were taken as $d_A = d_B = 100$ nm.

Transfer Matrix (*T-Matrix*) method has been adopted to simulate the optical response of the photonic devices and their corresponding EM density field distributions. As Eq. (1) shows, this method allows to relate plane wave amplitudes at jth layer at the z_j interface to the amplitudes of the $(j-1)$th layer at the same z_j, using 2×2 transfer matrices $M_j(z_j)$ and $M_{j-1}(z_j)$. A complete description of the *T-Matrix* method considerations is found in many Refs. [11,41]. Following this procedure to all layers, it is possible to associate transmitted and reflected plane wave amplitudes with the incident ones through a unique transfer matrix $\mathbb{M}$ that includes all the layers material information (e.g.: refractive indexes, thicknesses, propagation angles). In particular, in this work plane wave propagation is defined in normal incidence $\theta = 0°$ and a time dependence of $e^{i\omega t}$ has been considered. *T-matrix* method has been implemented in a Python program developed in the group, using standard scientific modules as *numpy*, *scipy* and *pandas*.

$$\begin{aligned}\begin{pmatrix} A_j \\ B_j \end{pmatrix} &= [M_j(z_j)]^{-1} M_{j-1}(z_j) \begin{pmatrix} A_{j-1} \\ B_{j-1} \end{pmatrix} = \\ &= [M_j(z_j)]^{-1} M_{j-1}(z_j) \dots \dots \\ &\dots \dots [M_2(z_2)]^{-1} M_1(z_2) \begin{pmatrix} A_{inc} \\ B_{inc} \end{pmatrix} = \\ &= \mathbb{M} \begin{pmatrix} A_{inc} \\ B_{inc} \end{pmatrix}\end{aligned} \tag{1}$$

This method allows to define the reflectance R as

$$R(\lambda) = \left| \frac{B_{inc}}{A_{inc}} \right|^2 = \left| \frac{\mathbb{M}_{21}}{\mathbb{M}_{11}} \right|^2 . \tag{2}$$

EM fields at each layer are calculated using the amplitudes A_j, B_j at each j layer.

3. Results and discussion

3.1. M-PhS-M structures

MIM structures can act as Fabry–Pérot resonator structures presenting characteristic valleys as a consequence of the multi-beam interference in the cavity which modulates reflectance and transmittance spectra of the structure. Fig. 1-ESI shows the $|\mathbb{E}|^2$ for a 600 nm SiO_2 film in between two Ag films of thickness $d_{M_1} = d_{M_2} = d_M = 25$ nm, where it is possible to observe the reflectance spectra that for $\lambda = 949; 636; 481$ nm exhibits resonances where constructive interference condition is fulfilled. For each one of these wavelengths a clear confinement of the $|\mathbb{E}|^2$ field distribution inside the cavity is observed. In [22], a quantum analogy through electronic orbitals is made to understand the electromagnetic (EM) field distribution inside the insulator layer distinguishing symmetric and anti-symmetric states in a quantum well but it is also possible to interpret these results via a mechanical analogy: the field shown in the insets of Figure 1-ESI resembles the oscillation modes of transverse standing waves in a string with both extremes fixed, where is possible to clearly distinguish resonance wavelengths as cavity modes at $\lambda_m = 2nd^*/m$ where n is the refractive index of the insulator and $m = 1, 2, \dots$ is an integer that numbers the modes. The thickness $d^* = d_{SiO_2} + 2d_p$ is defined as the total real thickness of the SiO_2 film plus d_p which corresponds to the penetration depth of the wave in the metal layer, being $d_p \approx 23$ nm for Ag in the optical range. In this resemblance, for example, $\lambda = 949$ nm corresponds to cavity mode $m = 2$ where it is easy to denote the node at the center of the SiO_2 slab. Analogously, it is possible to study the IM (*insulator–metal*) case of the same film onto only one metal Ag thin layer of $d_{M_2} = 25$ nm thickness ($d_{M_1} = 0$ nm). Reflectance spectra for this case (Fig. 2-ESI) shows the expected classic interference oscillations while $|\mathbb{E}|^2$ field denotes less confinement. Following the string analogy, the $|\mathbb{E}|^2$ field distribution can be associated with standing waves with *open-fixed* extremes where a maximum of the transversal string displacement is found at the open extreme. The Air-SiO_2 interface acts as the open extreme, since for each

Table 1
Lorenztian parameters table.

Structure	Fig	A	λ_0 (nm)	γ_0(nm)	Q_A	$\lvert\mathbb{E}_{max}\rvert^2$
$(LH)_3$-M	2a	0.53	908	72.7	6.7	8.10
$(HL)_2$H-M	2b	0.67	894	49.7	12.1	10.14
M-$(LH)_3$-M	2c	0.36	884	11.0	28.5	4.9
M-$(HL)_3$-M	2d	0.65	884	11.7	48.7	40.60
M-$(HL)_2$H-M	3a	0.98	821	13.1	67.5	10.82

Table 2
Sensibility S, Figure of Merit FOM and Q_A for the same studied PhS in Fig. 2 and 4 but considering mesoporous materials of 30%.

Structure	S (nm·RIU^{-1})	FOM (RIU^{-1})	Q_A
$(L^pH^p)_3$-M	131	1.14	4.2
$(H^pL^p)_2H^p$-M	112	1.68	10.9
M-$(L^pH^p)_3$-M	114	9.75	28.1
M-$(H^pL^p)_3$-M	114	10.0	44.1
M-$(H^pL^p)_2H^p$-M	97	7.32	50.0

resonance wavelength the $|\mathbb{E}|^2$ field exhibits a maximum. Resonances positions are observable in the plotted range at $\lambda_m = 4n\hat{d}/(2m-1)$, where for this case m is the integer of each mode and $\hat{d} = d_{SiO_2} + d_p$. From $|\mathbb{E}|^2$ field distributions is it easy to confirm that confinement is better achieved for *fixed-fixed* extremes than at *open-fixed* ones.

1D photonic crystals correspond to periodic asymmetric multilayer PhSs with well-known band-gap responses where high reflectance is obtained. Symmetric PhSs present similar optical response exhibiting small shifts in the band gap characteristics compared to the asymmetric case. For the four PhSs cases to be studied in Fig. 2(a) to (d), dotted light gray lines represent the reflectance of corresponding PhS. In all cases, it is possible to observe the presence of a first band-gap at $\lambda_{BG} \approx 821$ nm and the second one near 395 nm. In Fig. 2(a) it is shown in blue solid line the reflectance spectra of the $(LH)_3$-M structure. A clear valley is observable at (908 ± 35) nm due to the existence of a localized Tamm plasmon polariton mode inside of the band-gap. The localized mode is observed in the $|\mathbb{E}|^2$ intensity distribution where the field is clearly concentrated in the high-refractive index layer, TiO_2, next to the metal slab as already described elsewhere [31,42,43]. Fig. 2(b) shows the optical response but for a symmetric $(HL)_2H$ photonic structure followed by the metal layer ($(HL)_2$H-M structure). It is interesting to note that the reflectance response at the valley is almost located at the same wavelength, but exhibits a clearly higher resonance valley. Adding symmetry to the structure results into a more bounded interval of incidence wavelenghts for the $|\mathbb{E}|^2$ field as it is possible to observe in the localized mode. It is interesting to note, that in both Figs. 2(a) and (b), it is possible to observe a maxima of the $|\mathbb{E}|^2$ field at the boundary of the photonic structure with air, in complete analogy with the IM *open-fixed* extremes and with the corresponding string standing waves described above. In particular, the *open* extreme is better defined for the $(HL)_2H$ structure (Fig. 2(b)) due to the symmetry of the multilayer structure, giving rise to better resonance and confinement.

As discussed for Figs. 1 and 1-ESI, another strategy to increment to localization factor is shown in Fig. 2(c) where the same anti-symmetric multilayer structure of Fig. 2(a) is considered but the metal layer is not only included at the final of the structure but also at the beggining of it. For this case, *fixed-fixed* cavity modes clearly appear and Tamm resonance has a weaker valley but the localization in the wavelength of the $|\mathbb{E}|^2$ field is clearly enhanced at the high refractive index layer next to the top metal layer due to the two metal layers (*fixed-fixed* extremes). Moreover, Fig. 2(d) corresponds to the same combination of layers of Fig. 2(c) but with an inversion of order, being consequently the TiO_2 layer as the first layer of the structure in contact with the first metal layer. This case shows the same band gap structure of the multilayer as cases (a) and (c) but a clear sharper valley with an high increase in the $|\mathbb{E}|^2$ field confinement of 11 nm width is exhibited.

The spectral response of Tamm resonances is compatible to photonic resonances which clearly show an inverse Lorentzian lineshape as the one given by Eq. (3).

$$f(\lambda) = B - A\frac{1}{1+4\left(\frac{\lambda-\lambda_0}{\gamma_0}\right)^2}, \tag{3}$$

where $A = \frac{2\hat{A}}{\pi\gamma_0}$ represents the amplitude of the Lorentzian function with $\hat{A}$ the area under the peak and B is the parameter that inverts the Lorentzian function. λ_0 is the peak position of the Lorentzian function, while γ_0 is the scale parameter that specifies the full-width at half-maximum (FWHM). Each one of the Tamm resonances studied in Fig. 2 have been adjusted by the proposed function, in Fig. 4-ESI an example of one of them is exhibited showing an excellent fitting ($R^2 \approx 0.99$ for all cases). Fitting parameters are specified in Table 1 (in all cases $B \approx 1$) with which the quality factor $Q_A = \frac{A\lambda_0}{\gamma_0}$ has been calculated and informed in the last but one column of Table 1. The proposed quality factor allows the comparison of the structures among them as potential filter signals. Absolute $|\mathbb{E}_{max}|^2$ values are exhibited in the last column of Table 1. It is possible to deduce that although λ_0 and γ_0 are analogous as expected for structures M-$(LH)_3$-M and M-$(HL)_3$-M, the last but one row shows higher Q_A factor and higher $|\mathbb{E}_{max}|^2$, what makes this particular combination of stacks a potential good structure for its use as filter sensor and as an excellent platform for the inclusion of photoactive nanoentities in the TiO_2 layer.

To deepen into the potential use of these structures as sensors, the same 4 structures of Fig. 2 have been studied but considering mesoporous layers of 30% of porosity each. The porosity used in this section was chosen considering mean values of parameters already reported mesoporous PhCs synthesized by sol–gel methods [11,44,45]. These layers are now identified as L^p and H^p, for which their effective refractive index n_{eff} is a mixture of the refractive index of the matrix SiO_2 or TiO_2 respectively, and of the inhomogeneities whose refractive index is n_{inh}. In all cases, n_{eff} has been calculated using the Maxwell–Garnett approximation [46]. The mentioned porosity allows us to evaluate the performance of the devices according to parameters as the Sensibility $S = \Delta\lambda/\Delta n$ where $\Delta\lambda$ and Δn refer to the wavelength shift due to the refractive index change and the Figure Of Merit $FOM = S/\text{FWHM}$. Q_A for these porous systems has also been included for completeness of the study. In Table 2 it is possible to observe that the sensibility S of all the studied PhS is similar within a margin of 10%, being the classical Tamm structure the one of higher S due to the impedance conditions. However, when a shift occurs, it is also important to study the FOM since the resonance FWHM (represented by γ_0) allows to better distinguish the shift as a consequence of the better separation between valleys/peaks. In Table 2 it is possible to observe that the PhS that are embedded in two metals have a FOM nearly 10 times higher than PhSs with just one metal layer and that the Q_A for these PhS is also the higher ones as already observed in Table 1. In particular, Fig. 3 exhibits the resonance shifts for the same $(L^pH^p)_3$ substructure embedded in 1 or 2 metal layers. It is possible to observe a clear difference in the resonance FWHM. Also, it is possible to observe that the color change in the visible range according to the shifts in $(L^pH^p)_3$-M due to the increment of n_{inh} does vary significantly. Contrary, the M-$(L^pH^p)_3$-M in Fig. 3(b) shows a noticeable color change when n_{inh} changes from 1 to 2. The color simulation has been made following a CIE 1931 standard with D65 illuminant, using a home-made Python software developed in the group. The color corresponds to the transmittance spectra obtained for each structure.

In Fig. 4(a), both strategies for enhancement used for the studied cases of Fig. Fig. 2 were considered: symmetry of the multilayer structure and inclusion of both metal thin film endings. Thus, the same symmetric structure $(HL)_2H$ of Fig. 2b was studied embedded in two metal slabs ($d_{M_1} = d_{M_2} = 25$ nm) forming the M-$(HL)_2$H-M PhS. An analogue of this symmetric structure is analyzed by Durach et al. [47],

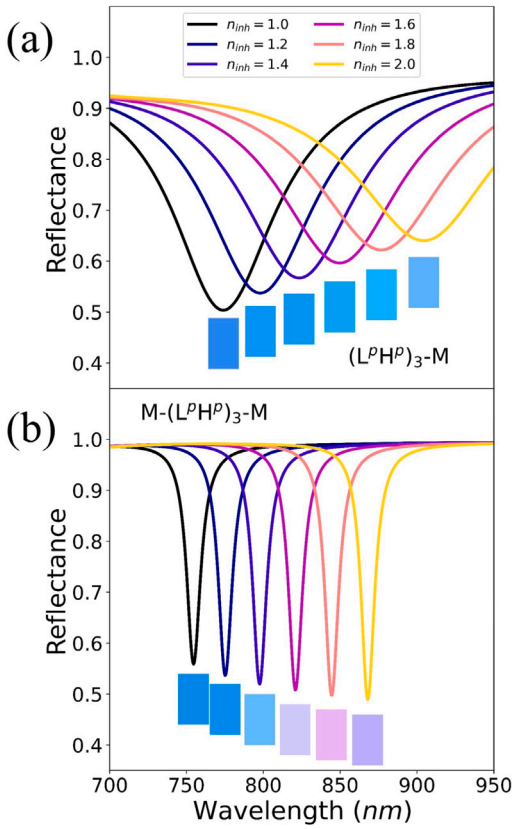

Fig. 3. Reflectance spectra for (a) $(L^pH^p)_3$-M system and (b) M-$(L^pH^p)_3$-M system. In both cases, the response of systems with 30% porosity is showed as a function of the refractive index of the inhomogeneity, n_{inh}. Also, the simulated color by transmittance is showed in each case.

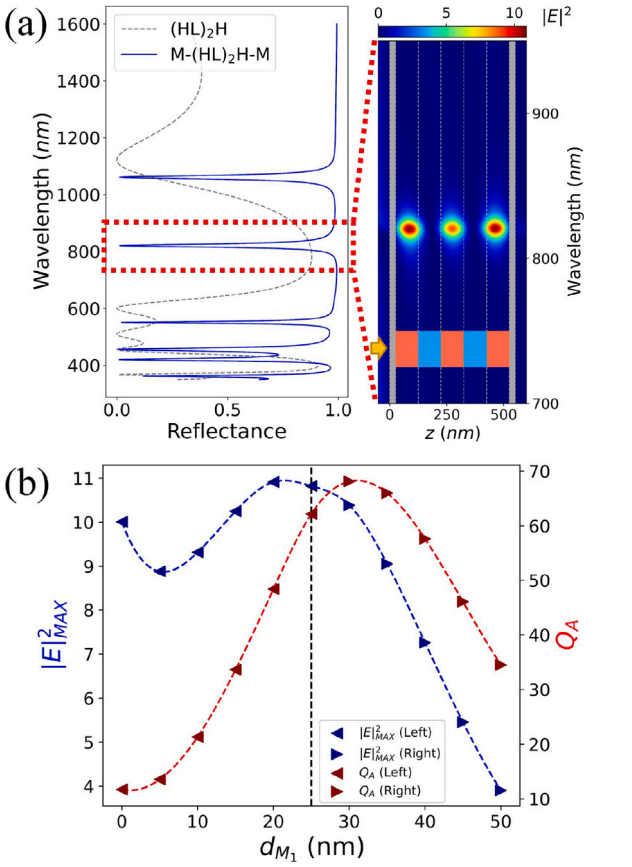

Fig. 4. (a) Reflectance spectra and $|\mathbb{E}|^2$ field distribution for the M-$(HL)_2$H-M system ($d_{M_1} = d_{M_2} = 25$ nm). (b) Effect of the thickness of the first metal layer (d_{M_1}) of the structure in the maximum field amplification $|\mathbb{E}|^2_{max}$ and the quality factor Q_A at the Tamm resonance.

where they describe the connection between cavity modes and TPPs in a system M-$(HL)_{20}$H-M. In our case, we observe that Q_A reaches the highest value among all the studied structures for the Tamm resonance which changes its position to $\lambda = 821$ nm which corresponds exactly to the center of the band gap of the photonic structure. However, this case shows an important decay of the $|\mathbb{E}_{max}|^2$ value as it is shown in the last row of Table 1. Unlike all $|\mathbb{E}_{max}|^2$ field distributions of all cases of Fig. 2, where it was possible to distinguish an intensification of the EM field at the TiO_2 layer next to the metal slab (whether the structure had one or two metal slabs) in what can be identified as a *single* Tamm, for the M-$(HL)_2$H-M structure it is possible to observe a double intensification of the field in both TiO_2 layers next to each metal slab at the beginning and at the end of the structure. This field spread over all layers is the reason why it is not possible to concentrate to such high values the $|\mathbb{E}|^2$, but denotes the presence of a *double* Tamm plasmon polariton. The field distribution resembles a Hermite function of order 2 which is in complete accordance to the cavity mode 3 expected for this type of structure. This result is confirmed in Fig. 3-ESI where the simulation of the same structure but for 11 layers was fulfilled observing the same tendency (Hermite function of order 5). It is important to denote that the terminology *double* Tamm does not infer the co-existence of two states but implies the characteristic Tamm intensification to both sides of the structure which will be of importance in the next section of this work. Results exhibited in Fig. 4(a), let us conclude that the sum of both conditions does not resume in a better platform for field confinement and Q_A at the same time. Fig. 4(b) shows the evaluation of the $|\mathbb{E}_{max}|^2$ and Q_A values as the thickness of one of the metal thin layers is modified. Evaluating $d_{M_1} = [0–50]$ nm allows modifying at the same time symmetry and confinement due to metal extremes. The evolution of Q_A shows clearly that increasing the symmetry of the whole structure by increasing the metal slab thickness, the Tamm resonance at the reflectance spectra shows a better signal to be used in sensor applications [34,35] reaching a maximum value for $d_{M_1} = 30$ nm which is not the symmetrical value expected, probably due to the incidence direction. However, this value does not coincide with the confinement of the localized mode. Confinement for $d_{M_1} \leq 25$ nm is located in the TiO_2 layer immediately before the last metal layer, for values $d_{M_1} \geq 30$ nm confinement changes to the TiO_2 layer immediately after the first metal layer but $|\mathbb{E}_{max}|^2$ value diminishes with the increment of d_{M_1} due to the increasing absorption of the metal layers.

3.2. MIM-PhS-MIM: Coupling modes due to symmetry

Coupling modes are obtained through the strategical combination of nanostructures. A hybrid 1D multilayered structure that combines the already analyzed M-PhS-M structures embedded in 2 MIM substructures result as an interesting potential platforms to couple modes in the sub-wavelength scale. Fig. 5 is a scheme for the MIM-PhS-MIM structures to be studied, where a MIM cavity is added before and after to any of the PhSs described in Fig. 2(c) and (d) and in Fig. 4. The central insulator in each MIM is SiO_2 of thickness d_I.

Fig. 6 shows 2D maps of hybrid MIM-PhS-MIM reflectance for thickness $d_I = [0–1000]$ nm as a function of wavelength. Each one of the 4 subplots shows the optical response of the different PhS analyzed in the previous section. The four Ag metal layers thickness involved in the simulation are $d_{M_x} = 12.5$ nm with $x = 1, 2$. So, the case $d_I = 0$ nm for which $2d_{M_x} = 25$ nm retrieves the metal layer thickness and the

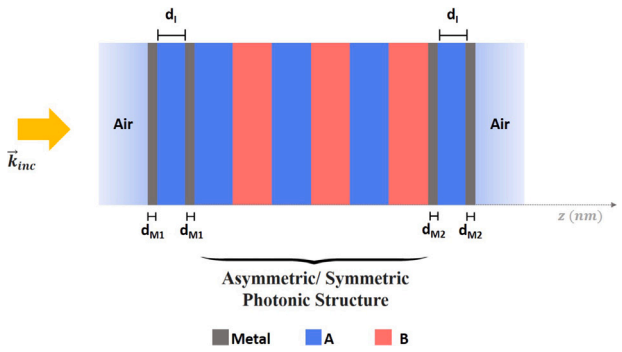

Fig. 5. Scheme of hybrid MIM-PhC-MIM photonic structures used in this work. The central PhC can be symmetric or anti-symmetric and the central dielectric material at each MIM substructure was the low index material (SiO_2 in our case) at all studied cases.

spectra of cases in Figs. 2(c), (d) and 4. In all cases, as d_I increases it is possible to observe the presence of reflectance branches. On one side, straight lines of increasing slope covering all wavelengths as d_I increases correspond to MIM cavity modes denoted in Fig. 6 as MIM branches. On another side, vertical quasi-continuous lines correspond to PhS cavity modes (CM) indicated in the figure as CM branches. These two branches combine and mix in several regions of the 2D map according to the electromagnetic response of the hybrid nanostructure. It is important to note that the presence of single or double Tamm plasmon polaritons modify significantly the expected behavior of the combination between the two types of states, as we shall see later.

In Fig. 6a, the M-$(HL)_2$H-M symmetric PhS analyzed in Fig. 4 has been embedded in the hybrid structure. For $d_I = 0$ nm at $\lambda = 2092; 1114; 821$ nm, it is possible to observe the three first CMs. The last two of this CMs have been already seen in Fig. 4. For the first cavity mode at $\lambda = 2092$ nm, for $d_I \approx 650$ nm a clear interaction between the cavity mode and the MIM 1 branch is observable. This interaction can be described analogously to the three-cavity resonator (2 MIM and the PhS) studied by Zappone et al. [26] which has been interestingly associated to quantum eigenstates of three quantum wells where the overlap of wavefunctions is not negligible. This overlap is namely allowed through the thickness of the metal layers selected to fulfill the condition $d_{M_x} < d_p$, where d_p is the penetration depth of the EM wave in the metal layer. So it is possible to define that the cavity states couple in a triplet state with bonding, and antibonding states symmetrically distributed. In Fig. 6a, this behavior repeats for the 4th PhS cavity mode at $\lambda = 600$ nm and $d_I \approx 100$ nm where it is also possible to observe that the same effect occurs for higher d_I thicknesses which excite higher orders of the MIMs cavity states.

For the case of the third PhS state, the one that has been studied in Fig. 4 denoting the existence of the double Tamm behavior, it can be seen that when $d_I < 100$ nm, the Tamm state is barely perturbed by the presence of MIMs. However, a different behavior is observable for 100 nm $< d_I <$ 400 nm, it is possible to observe a strong coupling behavior, giving place to a Rabi splitting around $d_I \equiv d_{RS} =$ 260 nm. In the vicinity of d_{RS}, 4 photonic states appear due to the rupture of degeneracy of MIM branch at the start and end of the MIM-PhS-MIM structure. The energy difference ΔE_{RS} at the anti-crossing splitting at d_{RS} can be defined from $\Delta\lambda_{RS} = \lambda_{RS}^{high} - \lambda_{RS}^{low}$ as $\Delta E_{RS} = hc\Delta\lambda_{RS}/(\lambda_{RS}^{high}\lambda_{RS}^{low})$. For Fig. 6(a), $\Delta E_{RS} \approx 134$ meV which is higher than for other optical hybrid structures [37] described in literature. It is interesting to note that this large anti-crossing splitting appears at the Tamm wavelength and not at other cavity modes. Congruently, a second anti-crossing splitting is also found at $\lambda = 443$ nm ($d_I \equiv d_{RS} = 95$ nm) which corresponds to the second order of the Tamm state located inside the second photonic band gap, denoted as Tamm 2 branch in Fig. 6.

Reflectance of MIM-PhS-MIM with asymmetric PhSs are showed in Fig. 6(b) and Fig. 6(c) centered at the splitting region. In this cases, M-PhS-M substructures can sustain a single Tamm where the $|\mathbb{E}_{max}|^2$ is localized mainly at the last TiO_2 layer (in the case $(LH)_3$) or in the first TiO_2 layer (in the case $(HL)_3$) as it was already shown in Fig. 2(c)

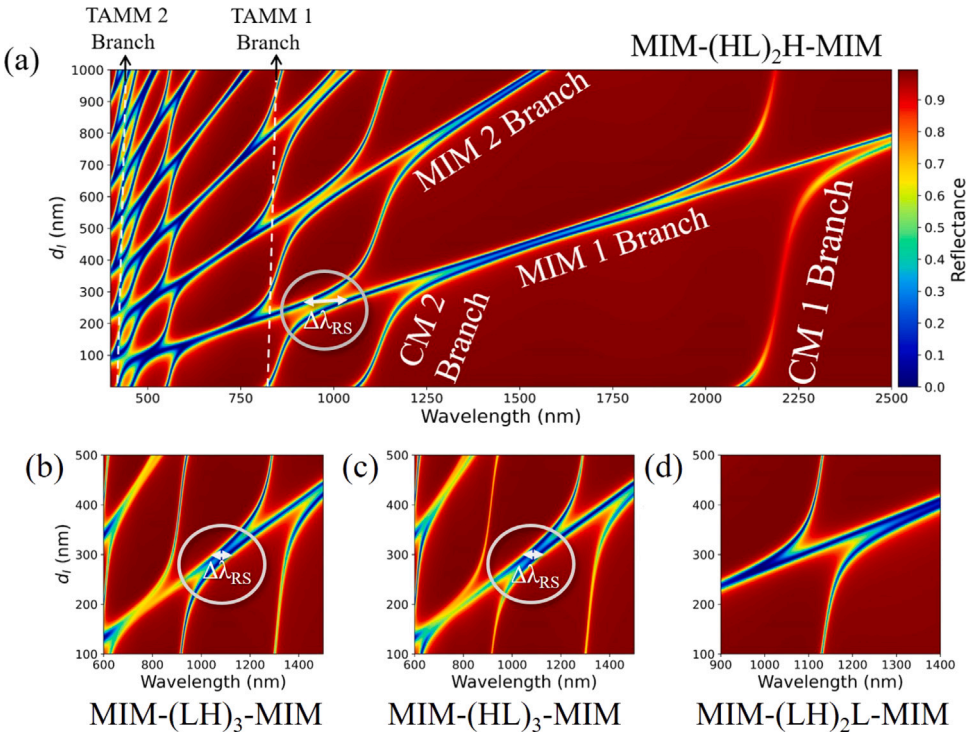

Fig. 6. Reflectance spectra of several MIM-PhC-MIM hybrid structures, as a function of the thickness of the central MIM insulator (d_I, $I = SiO_2$). (a) MIM-$(HL)_2$H-MIM (b) MIM-$(HL)_3$-MIM (c) MIM-$(LH)_3$-MIM (d) MIM-$(LH)_2$L-MIM. In (a), (b) and (c) $\Delta\lambda_{RS}$ is indicated.

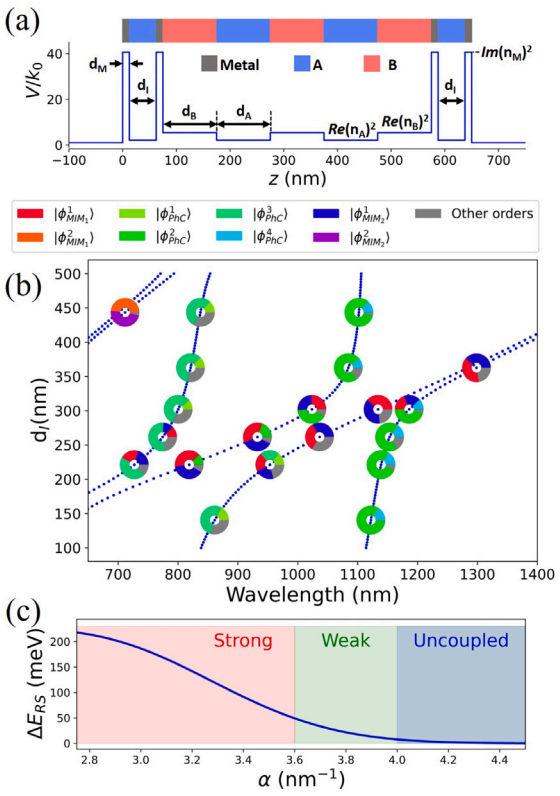

Fig. 7. (a) Optical potential used in the variational model. (b) Contribution to several eigenstates in the MIM-$(HL)_2$H-MIM hybrid structure, calculated using variational method. Cavity modes of MIM and PhC are used as basis of the calculation, by the use of Hermite functions centered in the MIM and PhC substructures. Each pie plot represent the contribution of each cavity state at this point. (c) ΔE_{RS} calculated according to the variational method as a function of α. (see eq. Eq. (5))

and (d). The general features described for the symmetric MIM-$(HL)_2$H-MIM structure are maintained. The position of the crossing between Tamm and MIM branches occurs at $d_{RG} = 310$ nm exhibiting an energy difference of $\Delta E_{RS} \approx 47$ meV at the hybridization anticrossing splitting, significantly lower respect to the one corresponding to the MIM-$(HL)_2$H-MIM structure analyzed in Fig. 6(a). This result evidences the fact that at the symmetric MIM-$(HL)_2$H-MIM the double Tamm is responsible for the wider Rabi splitting.

Finally by mean of completeness, the symmetric MIM-$(LH)_2$L-MIM structure is considered in Fig. 6d which cannot support Tamm states. Due to this condition, there is no rupture in the degeneracy of MIM cavity modes by the effect of crossing with PhS modes.

3.3. Variational method applied to MIM-PhC-MIM hybrid structures

A semi-quantitative Rayleigh–Ritz variational method [48] has been implemented to interpret the strong coupling of the optical modes that arise in the MIM-PhS-MIM structures described in the previous section. This type of analysis has been used before by Zappone et al. [26] applied to $(MI)_3M$ structures of several thicknesses. The model is based in the analogy between the Schrödinger and the Helmholtz equations,[22,26] given the optical Hamiltonian:

$$\hat{H} = \frac{d^2}{dz^2} + V(z) \tag{4}$$

where $V(z) = k_0[n(z) - ik(z)]^2$ is the optical potential of the system, $n(z)$ and $k(z)$ are the real and imaginary part of the refractive index of the system, respectively, and $k_0 = 2\pi/\lambda_0$ is the wavevector in the vacuum. In Fig. 7a, the optical potential $V(z)/k_0$ is shown for the M-$(HL)_2$H-M hybrid structure which is the one selected to show the analogy and understand the hybridization since it is the case identified of maxima splitting. In order to use the variational method, we need to conserve the hermeticity of the optical Hamiltonian. It is proved by Caliuguri et al. [22] that this condition is fulfilled if $n(z) \gg k(z)$ or $n(z) \ll k(z)$ at each z. In the case of Ag, this happens at $\lambda >$ 390 nm, when the imaginary part of the refractive index dominates its behavior. In the case of SiO_2 and TiO_2, the absorption is negligible at the considered wavelengths, and it is possible to take only the real part of its refractive index. The model is used to calculate the eigenstates for the MIM-PhS-MIM system as linear combinations of optical cavity modes, for both MIM and M-PhS-M substructures. The selected basis functions described in Eq. (5) are the normalized Hermite functions centered at each substructure which represent the electric field $\mathbb{E}$ at the cavity modes wavelengths of each substructure accordingly to what has been described for the field distribution in Fig. 4. The first 5 Hermite functions $\phi_q^{z_0}(z)$ and $[\phi_q^{z_0}(z)]^2$ are shown in Fig. 5-ESI as an example.

$$\phi_q^{z_0}(z) = \frac{\pi^{-1/4}\sqrt{\alpha}}{\sqrt{2^q q!}} e^{-\alpha^2(z-z_0)^2/2} H_q(\alpha(z - z_0)) \tag{5}$$

where q is the order of the Hermite function, α is the decay parameter of the function, z_0 is the center of the cavity and $H_p(x)$ is the Hermite polynomial of order p.

For MIM-PhS-MIM structures, the electric field $\mathbb{E}$ at all wavelenghts can be approximated as linear combination of the eigenstates as described by Eq. (6):

$$|\psi\rangle = \sum_{i=0}^{q_{MIM_1}} c_i^{MIM_1} |\phi_i^{MIM_1}\rangle + \sum_{i=0}^{q_{PhS}} c_i^{PhS} |\phi_i^{PhS}\rangle + \\ + \sum_{i=0}^{q_{MIM_2}} c_i^{MIM_2} |\phi_i^{MIM_2}\rangle, \tag{6}$$

where $|\psi\rangle$ is be the representation of the real electric field of the system in a given hybrid state. $|\phi_i^{MIM_1}\rangle$ and $|\phi_i^{MIM_2}\rangle$ is the identification for the first MIM before the PhS and for the MIM at the end of the whole structure respectively. q_{MIM_1}, q_{PhS} and q_{MIM_2} are the maximum order of the cavity modes in our systems, for each one of the MIMs and the PhS, while $c_i^{MIM_1}$, c_i^{PhS} and $c_i^{MIM_2}$ are the expansion coefficients that correspond to each basis function which will represent the contribution weight of each mode to compose the $\mathbb{E}$. These expansion coefficients and the eigenenergies are calculated solving the secular determinant:

$$\det(\mathbf{H} - E\mathbf{S}) = 0. \tag{7}$$

where $\mathbf{H}$ is the energy matrix with elements $H_{ij} = \langle\phi_i|\hat{H}|\phi_j\rangle$ and $\mathbf{S}$ is the overlap matrix, with elements $S_{ij} = \langle\phi_i|\phi_j\rangle$. The equation system was solved using numerical methods, using a Python program, using the standard *numpy* and *scipy* modules.

In order to account for the main features of the 2D reflectance spectra of Fig. 6a, we have proposed $q_{MIM_1} = q_{MIM_2} = 3$ and $q_{PhC} = 5$ as the maxima number of Hermite functions at each substructure. The refractive indexes used for the optical potential where $n_{Air} = 1$, $n_{Ag} = 6.37i$, $n_{SiO_2} = 1.45$ and $n_{TiO_2} = 2.33$, which correspond to the values at $\lambda = 900$ nm.

Fig. 7 shows the eigenenergies obtained with the variational model for the MIM-$(HL)_2$H-MIM hybrid structure, and the relative contribution of several basis functions at some points of the diagram. This contribution is calculated as $|c_i|^2/\sum_i |c_i|^2$, for each cavity mode used in the expansion. The proposed model shows the 2D reflectance plot calculated solving Eq. (7) in excellent accordance to what was obtained in Fig. 6a explicitly showing its principal splitting around $d_{RS} \approx 260$ nm.

This model permits to identify that the third and the fourth PhS cavity modes are the principal components of the third and fourth cavity modes as expected. Analogously, the MIM cavity modes act as the principal components of the branch that extends diagonally, i.e. from $(\lambda, d_I) = (600\text{ nm}, 150\text{ nm})$ to $(\lambda, d_I) = (1400\text{ nm}, 420\text{ nm})$. This branch correspond to the first MIM cavity mode of both $|\phi_1^{MIM_1}\rangle$ and

$|\phi_1^{MIM_2}\rangle$. For $\lambda > 1250$ nm, both MIM states are degenerated sharing the same eigenenergies, and correspond to the states $|\phi_1^{MIM_1}\rangle \pm |\phi_1^{MIM_2}\rangle$. These states do not interact between them by the existence of the PhS structure in the center of MIM-PhS-MIM system, causing the mentioned degeneracy. The same behavior is observable in the case of the second cavity modes of both MIMs, which appear in the branch that extends between $(\lambda, d_I) = (600\text{ nm}, 380\text{ nm})$ to $(\lambda, d_I) = (750\text{ nm}, 500\text{ nm})$.

As depicted in Fig. 6a, between $d_I = 150$ nm and $d_I = 350$ nm, the hybridization due to the strong coupling takes place due to the interaction of the first cavity modes of both MIMs and the third and fourth cavity modes of the PhS, which are mainly the components observable of the splitting. In particular, not only the first MIM states contribute to the states close to the vertical branches but also higher orders of MIM states showing a clear interaction of states to the splitting. It is also clear that the rupture of the degeneracy of the MIM cavity modes at the center of the anticrossing is mainly caused by the interaction of these states with PhS cavity modes, contributing with around a ∼20% to the hybrid states.

To obtain though the proposed model the 2D map of Fig. 6a, it was also necessary to define adequate values for the α parameter. The variation of this parameter denotes the degree of leakage of the proposed basis Hermite functions of each substructure in the other substructure. For high values of α, the function is more constrained to its respective substructure, while for low values, the function extends into the next substructure. Thus, the inverse of the α parameter is linear to the penetration distance of each substructure. Defining the proper value of α defines the type of splitting expected as shown in Fig. 7c where for values $\alpha > 4$ nm^{-1}, no coupling is expected, while for the interval [3.6–4] nm^{-1} a weak splitting can be observed similar to the one corresponding to Fig. 6d. For lower values than 3.6 a strong coupling is observable. In particular, to define a RS of the order of the one observed in Fig. 6a, α should be in [3.1–3.3] nm^{-1}. However, if we expect to re obtain the RS of the anti-symmetric structures of Fig. 6c and d, $\alpha \approx 3.6$ nm^{-1}.

The α parameter analysis confirms that there is a clear difference between the single and the double Tamm plasmon polariton behavior which denotes interplay with the MIM structures and consequently the strength of the anticrossing splitting.

4. Conclusions

In this work, we have shown how TPP resonances and electromagnetic field enhancement is modified according to the symmetry of a 1D photonic structure (PhS) which is embedded within the two metal slabs. The PhSs selected for this work were designed to include a low number of slabs that are representative of feasible experimental structures. Thus, we showed that symmetry control PhSs with bulk materials or with porous ones is a determinant factor in obtaining high-quality factor, good FOMs, and energy confinement in relation to the classical Tamm resonators. The increment in the quality factor goes up to 10 times higher for the M-$(HL)_2$H-M structure which implies at the same time a better spectral localization. For this case, the electromagnetic field enhancement shows almost no increment compared in contrast to the M-$(HL)_3$-M structure which increases up to 40 times the energy confinement in the dielectric with high refractive index with respect to the incident intensity. The great difference of energy confinement in both structures is due to the distribution of the electromagnetic field all along the photonic structure due to the existence of a double Tamm state as a consequence of the chosen symmetry. With the existence of single and double Tamm states, we were able to explain the coupling between two MIM structures at the beginning and at the end of the PhS. Clear hybrid TPP-MIM optical states were observable, where it was possible to define that strong coupling appears where Tamm states are available. In particular, the hybridization due to the strong coupling is higher for the double Tamm state in comparison with the single Tamm state. To understand the results a variational method was implemented to these structures which allowed us to confirm that the mode components of each structure are crossed at each branch of the hybrid structure, especially at the splittings. The degree of coupling was denoted by the α parameter which explains the role of the single/double Tamm states in the interplay between the two MIM structures.

The numerical results herein presented show that unlike the MIM-I-MIM studied in literature, having a MIM-PhS-MIM structure with Tamm states available does not only allow coupling between the PhS and the MIM but also a coherent coupling between the entrance and exit MIMs at the Tamm wavelengths. A tunneling is occurring consequently in the PhS, connecting directly both MIMs although the long distance given by the PhS. Considering that MIM structures resonances can be considered analogous to emitters, these results show that TPP modes within optoelectronic structures allow the coherent coupling of two emitters at the entrance and exit of an adequate PhS.

CRediT authorship contribution statement

Leandro Luis Missoni: Conceptualization, Methodology, Software, Formal analysis, Data curation, Investigation, Writing – original draft, Writing – review & editing, Visualization. **Guillermo Pablo Ortiz:** Conceptualization, Methodology, Review & editing. **María Luz Martínez Ricci:** Conceptualization, Methodology, Formal analysis, Writing – original draft, Writing – review & editing, Visualization, Supervision, Project administration, Funding acquisition.

Declaration of competing interest

The authors declare that they have no known competing financial interests or personal relationships that could have appeared to influence the work reported in this paper.

Data availability

Data will be made available on request.

Acknowledgments

This work was supported by Universidad de Buenos Aires, Argentina (UBACyT 20020190200245BA & 20020190100299BA) and CONICET funding PIP 11220210100205CO and by Universidad Nacional del Nordeste, Argentina (UNNE - PI-18F008). MLMR is a member of CONICET. Leandro Missoni thanks CONICET for the PhD fellowship.

Appendix A. Supplementary data

Supplementary material related to this article can be found online at https://doi.org/10.1016/j.omx.2023.100273.

References

[1] C. Gigli, G. Leo, All-dielectric χ (2) metasurfaces: recent progress, Opto-Electron. Adv. 5 (7) (2022) 210093–1.
[2] A.F. Koenderink, A. Alù, A. Polman, Nanophotonics: Shrinking light-based technology, Science 348 (6234) (2015) 516–521.
[3] J.A. Schuller, E.S. Barnard, W. Cai, Y.C. Jun, J.S. White, M.L. Brongersma, Plasmonics for extreme light concentration and manipulation, Nat. Mater. 9 (3) (2010) 193–204.
[4] H. Wu, Y. Gao, P. Xu, X. Guo, P. Wang, D. Dai, L. Tong, Plasmonic nanolasers: Pursuing extreme lasing conditions on nanoscale, Adv. Opt. Mater. 7 (17) (2019) 1900334.
[5] A.K. Sarychev, A. Ivanov, A. Lagarkov, G. Barbillon, Light concentration by metal-dielectric micro-resonators for SERS sensing, Materials 12 (1) (2018) 103.
[6] Z. Yuan, P.C. Wu, Y.-C. Chen, Optical resonator enhanced photovoltaics and photocatalysis: Fundamental and recent progress, Laser Photonics Rev. 16 (2) (2022) 2100202.

[7] K.-T. Lee, J.-H. Park, S.J. Kwon, H.-K. Kwon, J. Kyhm, K.-W. Kwak, H.S. Jang, S.Y. Kim, J.S. Han, S.-H. Lee, et al., Simultaneous enhancement of upconversion and downshifting luminescence via plasmonic structure, Nano Lett. 15 (4) (2015) 2491–2497.
[8] S.K. Singh, S. Mazumder, A. Vincy, N. Hiremath, R. Kumar, I. Banerjee, R. Vankayala, Review of photoresponsive plasmonic nanoparticles that produce reactive chemical species for photodynamic therapy of cancer and bacterial infections, ACS Appl. Nano Mater. 6 (3) (2023) 1508–1521.
[9] J.-P. Monchalin, Optical detection of ultrasound at a distance using a confocal Fabry–Perot interferometer, Appl. Phys. Lett. 47 (1) (1985) 14–16.
[10] G.C. Park, K. Park, Critically coupled Fabry–Perot cavity with high signal contrast for refractive index sensing, Sci. Rep. 11 (1) (2021) 19575.
[11] R.M. Gazoni, M.G. Bellino, M.C. Fuertes, G. Giménez, G.J. Soler-Illia, M.L.M. Ricci, Designed nanoparticle–mesoporous multilayer nanocomposites as tunable plasmonic–photonic architectures for electromagnetic field enhancement, J. Mater. Chem. C 5 (14) (2017) 3445–3455.
[12] M. Butt, S.N. Khonina, N. Kazanskiy, Recent advances in photonic crystal optical devices: A review, Opt. Laser Technol. 142 (2021) 107265.
[13] Y. Chen, Y. Yin, L. Ma, O.G. Schmidt, Recent progress on optoplasmonic whispering-gallery-mode microcavities, Adv. Opt. Mater. 9 (12) (2021) 2100143.
[14] P. Törmä, W.L. Barnes, Strong coupling between surface plasmon polaritons and emitters: a review, Rep. Progr. Phys. 78 (1) (2014) 013901.
[15] M.F. Limonov, M.V. Rybin, A.N. Poddubny, Y.S. Kivshar, Fano resonances in photonics, Nat. Photonics 11 (9) (2017) 543–554.
[16] M.C. Fuertes, F.J. López-Alcaraz, M.C. Marchi, H.E. Troiani, V. Luca, H. Míguez, G.d.A. Soler-Illia, Photonic crystals from ordered mesoporous thin-film functional building blocks, Adv. Funct. Mater. 17 (8) (2007) 1247–1254.
[17] G. Soler-Illia, P. Angelomé, M. Fuertes, A. Calvo, A. Wolosiuk, A. Zelcer, M. Bellino, E. Martínez, Mesoporous hybrid and nanocomposite thin films. a sol–gel toolbox to create nanoconfined systems with localized chemical properties, J. Sol-Gel Sci. Technol. 57 (2011) 299–312.
[18] M.E. Calvo, O. Sánchez-Sobrado, S. Colodrero, H. Míguez, Control over the structural and optical features of nanoparticle-based one-dimensional photonic crystals, Langmuir 25 (4) (2009) 2443–2448.
[19] Q. He, K.H. Ku, H. Vijayamohanan, B.J. Kim, T.M. Swager, Switchable full-color reflective photonic ellipsoidal particles, J. Am. Chem. Soc. 142 (23) (2020) 10424–10430.
[20] M. Aalizadeh, A.E. Serebryannikov, A. Khavasi, G.A. Vandenbosch, E. Ozbay, Toward electrically tunable, lithography-free, ultra-thin color filters covering the whole visible spectrum, Sci. Rep. 8 (1) (2018) 1–11.
[21] M. Kim, Y. Kim, K. Kim, W.-T. Huang, R.-S. Liu, J.K. Hyun, D.H. Kim, Gap surface plasmon-enhanced photoluminescence from upconversion nanoparticle-sensitized perovskite quantum dots in a metal–insulator–metal configuration under NIR excitation, J. Mater. Chem. C 10 (2) (2022) 532–541.
[22] V. Caligiuri, M. Palei, G. Biffi, S. Artyukhin, R. Krahne, A semi-classical view on epsilon-near-zero resonant tunneling modes in metal/insulator/metal nanocavities, Nano Lett. 19 (5) (2019) 3151–3160.
[23] V. Caligiuri, M. Palei, G. Biffi, R. Krahne, Hybridization of epsilon-near-zero modes via resonant tunneling in layered metal-insulator double nanocavities, Nanophotonics 8 (9) (2019) 1505–1512.
[24] W. Qiu, L. Zhou, Y. Wang, X. Jiang, C. Huang, L. Zhou, Q. Zhan, J. Hu, Strong coupling of multiple optical interface modes with ultra-narrow linewidth in one-dimensional topological photonic heterostructures, Opt. Express 31 (12) (2023) 20457–20470.
[25] K. Hirai, J.A. Hutchison, H. Uji-i, Molecular chemistry in cavity strong coupling, Chem. Rev. (2023).
[26] B. Zappone, V. Caligiuri, A. Patra, R. Krahne, A. De Luca, Understanding and controlling mode hybridization in multicavity optical resonators using quantum theory and the surface forces apparatus, ACS Photonics 8 (12) (2021) 3517–3525.
[27] F.J. Garcia-Vidal, C. Ciuti, T.W. Ebbesen, Manipulating matter by strong coupling to vacuum fields, Science 373 (6551) (2021) eabd0336.
[28] H. Wang, H.-Y. Wang, A. Bozzola, A. Toma, S. Panaro, W. Raja, A. Alabastri, L. Wang, Q.-D. Chen, H.-L. Xu, et al., Dynamics of strong coupling between J-aggregates and surface plasmon polaritons in subwavelength hole arrays, Adv. Funct. Mater. 26 (34) (2016) 6198–6205.
[29] K. Pang, H. Li, G. Song, L. Yu, Strong coupling in silver-molecular J-aggregates-silver structure sandwiched between two dielectric media, Chin. Phys. B 28 (12) (2019) 127301.
[30] H. Wang, H.-Y. Wang, A. Toma, T.-a. Yano, Q.-D. Chen, H.-L. Xu, H.-B. Sun, R. Proietti Zaccaria, Dynamics of strong coupling between CdSe quantum dots and surface plasmon polaritons in subwavelength hole array, J. Phys. Chem. Lett. 7 (22) (2016) 4648–4654.
[31] M. Kaliteevski, I. Iorsh, S. Brand, R. Abram, J. Chamberlain, A. Kavokin, I. Shelykh, Tamm plasmon-polaritons: Possible electromagnetic states at the interface of a metal and a dielectric Bragg mirror, Phys. Rev. B 76 (16) (2007) 165415.
[32] R. Tamm, Pegelmessungen an fernsprechleitungen meßmethoden, Tech. Mess. tm 25 (JG) (1933) 279–280.
[33] R. Brückner, V. Lyssenko, S. Hofmann, K. Leo, Lasing of Tamm states in highly efficient organic devices based on small-molecule organic semiconductors, Faraday Discuss. 174 (2014) 183–201.
[34] M.C. Sansierra, J. Morrone, F. Cornacchiulo, M.C. Fuertes, P.C. Angelomé, Detection of organic vapors using Tamm mode based devices built from mesoporous oxide thin films, ChemNanoMat 5 (10) (2019) 1289–1295.
[35] B. Auguié, M.C. Fuertes, P.C. Angelomé, N.L. Abdala, G.J. Soler Illia, A. Fainstein, Tamm plasmon resonance in mesoporous multilayers: toward a sensing application, Acs Photonics 1 (9) (2014) 775–780.
[36] C. Kar, S. Jena, D.V. Udupa, K.D. Rao, Tamm plasmon polariton in planar structures: A brief overview and applications, Opt. Laser Technol. 159 (2023) 108928.
[37] J. Yang, H. Zhang, T. Wang, I. De Leon, R.P. Zaccaria, H. Qian, H. Chen, G. Wang, Strong coupling of Tamm plasmons and Fabry-Perot modes in a one-dimensional photonic crystal heterostructure, Phys. Rev. A 18 (1) (2022) 014056.
[38] P.B. Johnson, R.-W. Christy, Optical constants of the noble metals, Phys. Rev. B 6 (12) (1972) 4370.
[39] I.H. Malitson, Interspecimen comparison of the refractive index of fused silica, Josa 55 (10) (1965) 1205–1209.
[40] T. Siefke, S. Kroker, K. Pfeiffer, O. Puffky, K. Dietrich, D. Franta, I. Ohlídal, A. Szeghalmi, E.-B. Kley, A. Tünnermann, Materials pushing the application limits of wire grid polarizers further into the deep ultraviolet spectral range, Adv. Opt. Mater. 4 (11) (2016) 1780–1786.
[41] A. Yariv, P. Yeh, Electromagnetic propagation in periodic stratified media. II. Birefringence, phase matching, and x-ray lasers, JOSA 67 (4) (1977) 438–447.
[42] M. Sasin, R. Seisyan, M. Kalitteevski, S. Brand, R. Abram, J. Chamberlain, A.Y. Egorov, A. Vasil'Ev, V. Mikhrin, A. Kavokin, Tamm plasmon polaritons: Slow and spatially compact light, Appl. Phys. Lett. 92 (25) (2008) 251112.
[43] C. Kar, S. Jena, D.V. Udupa, K.D. Rao, Tamm plasmon polariton in planar structures: A brief overview and applications, Opt. Laser Technol. 159 (2023) 108928.
[44] D. Onna, M.C. Marchi, M.L. Martinez Ricci, S.A. Bilmes, Loading insoluble sulfides in mesoporous oxide films from precursors in solution, J. Sol-Gel Sci. Technol. 102 (1) (2022) 264–278.
[45] M. Fuertes, M. Marchena, M. Marchi, A. Wolosiuk, G. Soler-Illia, Controlled deposition of silver nanoparticles in mesoporous single-or multilayer thin films: from tuned pore filling to selective spatial location of nanometric objects, Small 5 (2) (2009) 272–280.
[46] A. Sihvola, Two main avenues leading to the Maxwell Garnett mixing rule, J. Electromagn. Waves Appl. 15 (6) (2001) 715–725.
[47] M. Durach, A. Rusina, Transforming Fabry-Perot resonances into a Tamm mode, Phys. Rev. B 86 (23) (2012) 235312.
[48] I.N. Levine, D.H. Busch, H. Shull, Quantum Chemistry, Vol. 6, Pearson Prentice Hall Upper Saddle River, NJ, 2009.